Chemical Engineering Journal 471 (2023) 144569

Contents lists available at ScienceDirect

Chemical Engineering Journal

journal homepage: www.elsevier.com/locate/cej

Activation of 2D cobalt hydroxide with 0D cobalt oxide decoration for microplastics degradation and hydrogen evolution

Rossella Greco [a,*], Lucía Baxauli-Marin [a], Filipp Temerov [a], Matyas Daboczi [b], Salvador Eslava [b], Yuran Niu [c], Alexei Zakharov [c], Meng Zhang [d], Taohai Li [a,e], Wei Cao [a,*]

[a] Nano and Molecular Systems Research Unit, Faculty of Science, University of Oulu, FIN 90014, Oulu, Finland
[b] Department of Chemical Engineering and the Centre for Processable Electronics, Imperial College London, London SW7 2AZ, UK
[c] MAX IV Laboratory, Lund University, Lund 22484, Sweden
[d] School of Physics, East China University of Science and Technology, Shanghai 200237, China
[e] College of Chemistry, Key Lab of Environment Friendly Chemistry and Application in Ministry of Education, Xiangtan University, Xiangtan 411105, China

ARTICLE INFO

Keywords:
Cobalt hydroxide
Cobalt oxide
Photocatalysis
Microplastic degradation
Hydrogen evolution reaction

ABSTRACT

The 2D semiconductors are important players in environmental and energy fields due to their unique catalytic and physical properties defined by their dimensionality. Versatile functionalities on one 2D matrix will enlarge its application scopes but require dedicated engineering paths. In this work, we present a cross-dimensional strategy by decorating 0D Co_3O_4 onto 2D $Co(OH)_2$ to form a multifunctional photocatalyst. The one-pot hydrothermally synthesized Co_3O_4@$Co(OH)_2$ composite is capable of degrading polystyrene microplastics with an efficiency of 40% under 0.495 W white LED illumination. In a separated experiment, H_2 evolution reaction from water splitting was evaluated in absence of sacrificial agents leading to 43 μmol g^{-1} and to an apparent quantum efficiency of 3.48% at 420 nm. The study of the energy band diagrams by UV–Visible and ambient photoemission spectroscopy and the analysis of the radicals involved in the reaction of photocatalytic degradation allow to unveil the mechanisms for both the processes herein studied. Finally, we could confirm that the heterostructure benefits the redox potentials of 2D and 0D counterparts and facile electron transfers when crossing two different dimensions. These results provide guidelines and inspiration for cross-dimensional activations of low-dimensional materials for versatile functionalities.

1. Introduction

Two of the biggest issues hampering human's development are pollution and energy crisis. Despite numerous efforts, tackling the pollutants in wastewater associated with industrialization and urbanization also consumes energies, within which a large portion exist in unsustainable forms. Photocatalysis, utilizing light and photocatalysts, have been considered as a key alternative that may result in simultaneous remediations of pollution and clean solar fuel production [1]. Apart from "infinite" solar energy for human's proposal, photocatalysis heavily relies on the catalytic media, the photocatalysts [2]. In addition, differently from hydrogen evolution with the hydrogen as the targeted product, the pollutants surrounding human varying in species and chemical forms yet require specifications of their occurrence and hazardousness.

Microplastics (MPs), defined as plastic particles with a size lower than 5 μm [3], are some of the most worrying water contaminants [4]. The accumulation of these particles in oceans represents a great threat for the marine life ecosystem, due to their possible accumulation in fish organs and the consequent introduction in the food chain with scary but not yet clear consequences [5,6]. For these reasons, different methods have been applied for the degradation of these tiny but dangerous species. One of the possible approaches for avoiding the increase of these entities in natural environment is the photocatalytic degradation [7]. Up to now, the photocatalytic degradation of MPs has been reported on wide bandgap semiconductor matrices, e.g., TiO_2 and ZnO [8–11]. Despite the bandgap configurations are not in favour of visible light absorption, these oxide matrices require dedicated modifications to reach efficient MPs removals [12,13]. The new era of discoveries is pushing to explore narrow bandgap materials, in the visible range, to enable a wider solar irradiance activity in the urgent MPs remediation.

The uniqueness of 2D semiconductor materials, such as graphene,

* Corresponding authors.
E-mail addresses: rossella.greco@oulu.fi (R. Greco), wei.cao@oulu.fi (W. Cao).

https://doi.org/10.1016/j.cej.2023.144569
Received 25 April 2023; Received in revised form 27 June 2023; Accepted 1 July 2023
Available online 3 July 2023

MoS_2 or BN, and their different chemical-physical properties compared to their 3D counterparts are well-known. One of their most studied features has been the bandgap and the possibility of engineering it by changing the number of layers composing the materials [14]. Since 40% of sunlight is visible light, 2D materials might represent the new class of visible-light active photocatalysts, by tuning their optical properties. Furthermore, 2D materials will be endowed with higher surface areas compared to the bulk and this will allow to design the right catalyst and increase its applicability in photocatalysis [15,16]. The latter can be ensured also by the synthesis of composites of different photocatalysts, as a solution to the undesired electron-hole (e^--h^+) recombination [17].

Among several catalysts, cobalt compounds have been known for their exceptional magnetic and electrical properties, which led to a wide use of this metal in supercapacitors and batteries [18–26]. Moreover, cobalt has drawn the attention as main metal in different catalytic systems, especially for catalyzing organic reactions [27–33], oxidation reactions [34–43], and water splitting reaction [44]. The high electron-capture efficiency of cobalt makes its compounds active in several electrocatalytic [41–43,45–49] and photocatalytic reactions [50–54]. Belonging to one of the representative 2D families [55], $Co(OH)_2$ has been widely used for electrocatalysis [56–58] and identified active also in photocatalytic OER [59], theoretically accomplishing only half of the water splitting. The use of suitable counterparts to construct a heterostructure system allows to decrease the e^--h^+ recombination by improved charge-carrier separation. Co_3O_4 is a possible counterpart for its previously reported activity in hydrogen evolution [60,61]. The possibility to combine it with the 2D hydroxide counterpart has been demonstrated through one-pot hydrothermal synthesis and supercapacitor electrodes were constructed [62]. Furthermore, both Co_3O_4 and $Co(OH)_2$ possess bandgaps in visible light, 2.2 eV [63] and 2.3 eV [64], respectively. Proper engineering them into one composite may lead to new openings of photocatalytic MPs removal along with hydrogen evolution.

Herein, we present the combination of Co_3O_4 nanoparticles with 2D $Co(OH)_2$ slabs to form a dual-functional Co_3O_4@$Co(OH)_2$ photocatalyst for MPs removal and hydrogen evolution under visible light. Two cobalt components of the composite can be varied and combined by modulating the synthetic conditions in the facile one-pot hydrothermal synthesis. The synthesized Co_3O_4@$Co(OH)_2$ represents the first example of composite active in the photocatalytic degradation of polystyrene (PS) MPs in water, meanwhile the hydroxide $Co(OH)_2$ and the oxide Co_3O_4 had no activity in the above-mentioned reaction. A MPs weight loss of 40% was achieved upon 9 days of white-light LED irradiation. Moreover, the composite also showed activity in the photocatalytic hydrogen evolution in a separate experiment with an apparent quantum efficiency (AQE) of 3.48% at 420 nm without involvements of any scavenger or co-catalyst. The superior activity of the 0D@2D Co_3O_4@$Co(OH)_2$ is due to improved charge separation upon type-II heterostructure composite formation, which was demonstrated by measurements of photocurrent in constructed films, work function by Kelvin probe, and energy bands by ambient photoemission spectroscopy (APS) and UV–visible (UV–Vis) spectroscopy, confirmed by density functional theory.

2. Experimental

2.1. Preparation of catalysts

All chemicals were purchased with analytical grade from Sigma-Aldrich and used without further purification. $Co(NO_3)_2{\cdot}6H_2O$ (0.5 mmol) and polyethylene glycol-6000 (PEG-6000) (0.5 g) were stirred in H_2O (20 mL) for 30 min. Afterwards, aqueous NaOH (10 w/v%) was added dropwise to reach the desired pH values in order to yield the oxide, hydroxide or combination of them in the heterostructure form (pH = 9 for Co_3O_4, pH = 12 for Co_3O_4@$Co(OH)_2$ and $Co(OH)_2$). Then, the solution was stirred for 10 min. Next, the mixture at the correct pH value was introduced in a Teflon-lined stainless-steel autoclave and underwent hydrothermal treatment for 24 h at different temperatures: 140 °C for Co_3O_4@$Co(OH)_2$ (pH = 12) or 180 °C for Co_3O_4 (pH = 9) and $Co(OH)_2$ (pH = 12). Subsequently, the autoclave was naturally cooled down to room temperature. The dispersion was centrifuged at 3000 rpm for 40 min and then washed with water and ethanol (twice) and each time centrifuged at 3000 rpm for 40 min. Finally, the obtained solid was dried under vacuum overnight and characterized by different techniques (see SI Section 1.1).

2.2. Microplastic photodegradation

The PS MPs suspension was purchased from microParticles GmbH, with a concentration of 5 mg/mL and an average diameter of 0.9 μm. In a typical reaction, the catalyst (4 mg) was added to an aqueous suspension of PS MPs at a concentration of 2.5×10^{-3} w/v%. Then, it was irradiated under stirring for 9 days with a white-light LED (0.495 W) in a photoreactor Perfect Light PCX50B. The MPs photocatalytic degradation was evaluated by scanning electron microscopy (SEM). The formation of products from the degradation of the plastics was evaluated by liquid chromatography-mass spectrometry (LC-MS). The latter was performed using a Waters Synapt G2 HDMS Q-Tof system equipped with an ACQUITY UPLC® BEH C18 1.7 μm column (2.1 mm × 100 mm). CH_3COONH_4 (10 mM) and CH_3CN were used as mobile phase with a flow of 0.2 mL/min and composition of 50% of CH_3COONH_4 for 5 min, decreased to 5% for the following 5 min.

2.3. Hydrogen evolution reaction experiments

In a typical reaction, H_2O (10 mL) was placed in a quartz reactor with the catalyst (8 mg). The solution was kept stirring in dark conditions for 1 h while purging with argon. Then, it was irradiated under stirring for 6 h with a white-light LED with a power of 0.495 W in the Perfect Light PCX50B. The H_2 production was evaluated by gas-chromatography (GC) using an Agilent 8860 GC System, equipped with a split/splitless inlet, a TCD detector and a capillary column CP-Molsieve 5 Å 25 m × 0.53 mm × 50 μm.

3. Results and discussion

This section includes detailed results and investigations of prepared samples and their photocatalytic functionalities. The characterization results are presented in Section 3.1 to have a comprehensive understanding of sample properties, such as morphology, crystal structure, chemical compositions, and band energy diagram. To probe the possible photocatalytic capability, the optical and photoelectrical responses are studied and detailed in subsection 3.2. The photocatalytic activities and mechanistic studies are shown in the last subsection 3.3. First, results for MPs degradations and hydrogen evolution are quantitatively given. Then the density functional theory calculation was performed and elucidated to probe composite's electronic structures which are crucial for mechanistic studies. Finally, based on experimental determinations and DFT results, the photocatalytic mechanisms are elucidated for the MPs degradation, hydrogen evolution, and the connections between these two processes.

3.1. Characterization of Co_3O_4@$Co(OH)_2$

The Co_3O_4@$Co(OH)_2$ composite was synthesized by a hydrothermal method and the structural and chemical-physical properties were characterized by high resolution–transmission electron microscopy (HR-TEM), powder X-Ray diffraction (PXRD), and X-ray photoelectron spectroscopy (XPS). Fig. 1a and S1 show the TEM and SEM images, respectively. The obtained material exhibits form of cubic nanoparticles of Co_3O_4 supported on hexagonal nanoplates composed by $Co(OH)_2$. The selected area diffraction (SAED) pattern shown in Fig. 1b confirms the presence of both compounds in the composite. $Co(OH)_2$ is oriented

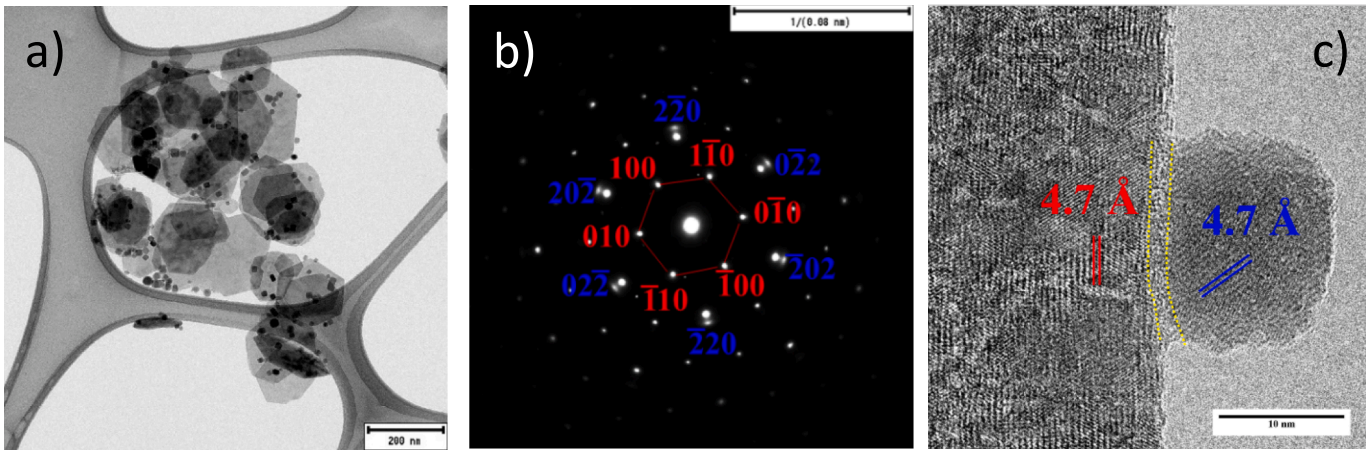

Fig. 1. (a) TEM micrograph of Co_3O_4@$Co(OH)_2$ and (b) SAED pattern, in red for $Co(OH)_2$ and in blue for Co_3O_4 and (c) HR-TEM micrograph of Co_3O_4@$Co(OH)_2$ (yellow lines represent the interfacial region). (For interpretation of the references to color in this figure legend, the reader is referred to the web version of this article.)

on the (0 0 1) plane and Co_3O_4 on the (1 1 1) plane, showing a hexagonal phase too. The presence of double spots in the SAED is related to the continuous growth of Co_3O_4 under the electron beam, when using high resolution. Consequently, the SAED pattern suggests that the nanoparticles are keeping the same phase of the hydroxide, due to the oxidation process of $Co(OH)_2$ [65], which is expected to be enhanced under the electron beam. This is also confirmed by the analysis of the lattice fringes of the two components by HR-TEM. Fig. 1c shows that in both cases the distances are ~ 4.7 Å, This value agrees with one for the (0 0 1) plane of β–$Co(OH)_2$ [66]. On the other hand, it differs from the previously reported value of 2.8 Å for (2 2 0) plane of Co_3O_4 [67], but related to (1 1 1) plane of the oxide. Not only does the HR-TEM image confirm a different crystallization orientation for Co_3O_4, directly connectable to the diffraction pattern of the pristine $Co(OH)_2$, but also the presence of a strict relation between the two components of the composite. Indeed, an interphase is present between the two bonded cobalt-based compounds as marked between two dashed yellow lines in Fig. 1c, acknowledging the presence of a phase boundary between the hydroxide and the oxide [68]. It is noted that a higher resolution TEM image than the current one is not feasible in the current setup due to radiation damage of the hydroxide by the electron beam at a high voltage and long exposure time as shown in Fig. S1b.

The occurrence of the two compounds in the material was confirmed by PXRD, as shown in Fig. S2a, by comparing them with the simulated results. A total absence of amorphous phase is detected and the typical peaks associated to the pure compounds, i.e., the brucite-like $Co(OH)_2$ and the spinel Co_3O_4, are visible. Indeed, the peaks at 22.3°, 37.8°, 44.2°, 45.2°, 60.2°, 68.4°, 72.9°, 81.2° and 83.0° can be indexed to the (0 0 1), (1 0 0), (1 0 1), (0 0 2), (1 0 2), (1 1 0), (0 0 3), (2 0 0) and (1 0 3) planes of $Co(OH)_2$, respectively [69]. On the other hand, the 36.2°, 42.9°, 65.6° and 77.5° are indexed to the (2 2 0), (3 1 1), (4 0 0) and (4 4 0) planes of Co_3O_4, respectively [67]. Furthermore, by using the RIR (reference intensity ratio) method it was possible to preliminarily quantify the ratio between Co_3O_4:$Co(OH)_2$, which was found to be 1.5:8.5.

The 0D@2D feature of the Co_3O_4@$Co(OH)_2$ composite was confirmed in microstructural and morphological characterizations. It was noticed that the XRD peaks are broadened in the Co_3O_4@$Co(OH)_2$ composite, compared with the simulated results in Fig. S2. The broadening is a typical feature of the nanocrystalized materials. The average nominal size for the Co_3O_4 nanoparticles was calculated from Fig. S3 to 15.01 nm through the TEM image of Fig. 1a, denoting a rather small size of the oxide enabling its categorization as 0D nanoparticles [70]. It is noteworthy that the nominal size of the nanomaterials is generally larger than the mean crystalized size [71], despite the latter is hardly obtained here due to the XRD peaks low intensity and the partial overlapping with these from hydroxides. By HR-TEM in Fig. S4, the thickness was calculated as ~ 9 nm, corresponding to around 20 layers. In fact, the thickness proves the 2D feature of hydroxide whose nanosheets are consisted of few layers.

Moreover, we demonstrate that it was possible to obtain pure oxide and hydroxide by modulating the reaction conditions. The samples prepared at the temperature of 180° but at different pH values of 9 or 12 exhibit pure oxide or hydroxide structures, as confirmed by the PXRD analysis in Fig. S2b and Fig. S2c. As in the composite, the pure $Co(OH)_2$ presents a hexagonal symmetry in form of nanoplates with a similar size distribution to the plates in the heterostructure (Fig. S5 and S6). In addition, Co_3O_4 could be synthesized in form of nanocubes (Fig. S7) by changing the pH to 9.

Fig. 2a–c and Fig. S8 display the XPS spectra of the samples in the Co 2p region and as total surveys, respectively. As described in the literature, the spectrum of cobalt presents two sets of signals related to the spin–orbit splitting into $2p_{1/2}$ and $2p_{3/2}$, which are also accompanied by satellite peaks [72]. The Co $2p_{3/2}$ binding energies are summarized in Table S1. It is noticed that the as-synthesized Co_3O_4@$Co(OH)_2$ presents features closer to $Co(OH)_2$. However, in Fig. 2a–c it is evident that the ratio between the signal at 780.0 eV and the one at 782.0 has decreased. Indeed, the peak at 780.0 eV is related in Co_3O_4 to the Co^{3+} and the enhanced feature of this peak might indicate the presence of Co^{3+}. Additionally, synchrotron radiation-based X-ray absorption spectroscopy (XAS) was used to further demonstrate the presence of the heterostructure. Fig. S9 shows that the pure $Co(OH)_2$ was converted into Co_3O_4 by the intensive X-ray radiation. However, a shoulder at 778 eV was recorded for the Co_2O_3@$Co(OH)_2$ composite, and can be assigned to the XAS feature of the octahedral Co^{2+} in $Co(OH)_2$ [73]. This demonstrates the beneficial role of the composite, where $Co(OH)_2$ is more radiation resistant, making the analysis possible by this technique. This is differently from the pure $Co(OH)_2$, where the typical feature at 778 eV was extremely diminished and the compound was almost totally transformed to Co_3O_4.

3.2. *Optical and photoelectric properties of Co_3O_4@$Co(OH)_2$*

The optical and energetic properties of the materials were determined by UV–Vis spectrophotometry and APS. Fig. 2d underlines the presence of the d-d transitions of Co^{2+} around 500 nm [54] and a band around 800 nm [74]. In addition, the Tauc plots (Fig. S10) allow to calculate the bandgaps of the materials as 1.70 eV for Co_3O_4 and 1.93 eV for $Co(OH)_2$. The valence band edge (E_v) values were determined by APS, and the Fermi levels (E_F) were taken from the equilibrium dark

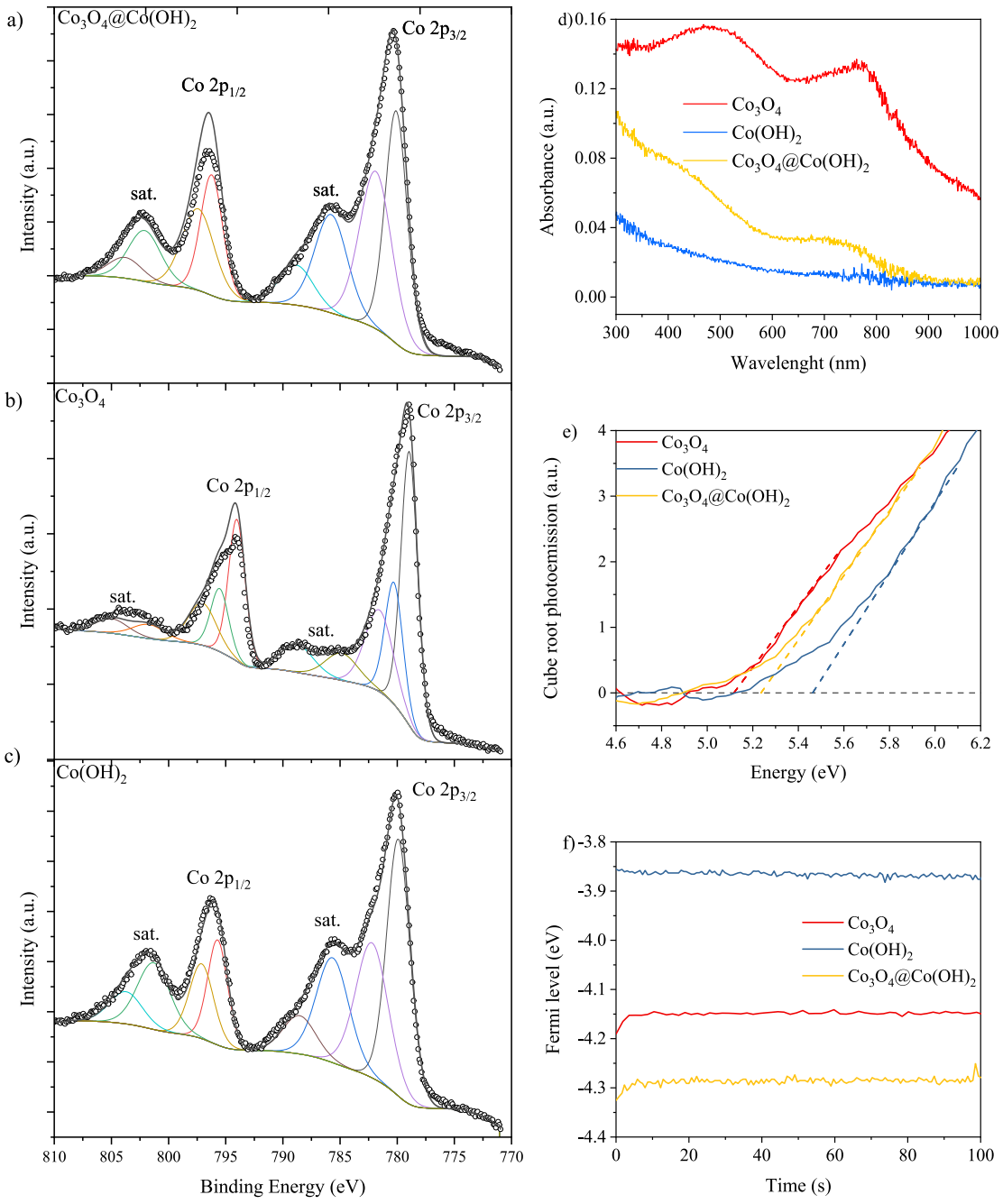

Fig. 2. High-resolution XPS spectra in the Co 2p region of (a) Co_3O_4@$Co(OH)_2$, (b) Co_3O_4 and (c) $Co(OH)_2$. d) UV–Vis spectra of Co_3O_4@$Co(OH)_2$, Co_3O_4 and $Co(OH)_2$ in water suspensions. e) APS of Co_3O_4@$Co(OH)_2$, Co_3O_4 and $Co(OH)_2$. f) Fermi levels of Co_3O_4@$Co(OH)_2$, Co_3O_4 and $Co(OH)_2$ obtained by Kelvin probe measurements.

work function values measured by Kelvin probe [75]. Consequently, the conduction band edge (E_c) values of the materials were calculated from the E_v values and the optical bandgaps of the semiconductors. As showed in Fig. 2e, the E_v for Co_3O_4 and $Co(OH)_2$ were measured at −5.12 eV and −5.46 eV, respectively, in good agreement with previous reports [76,77]. Taking into account the Fermi levels, Co_3O_4 is almost an intrinsic semiconductor, while $Co(OH)_2$ is a n-type semiconductor (see Fig. 2f and Table S2). The deeper E_F of Co_3O_4 (−4.15 eV) compared to the E_F of $Co(OH)_2$ (−3.86 eV) will result in the formation of a downward (towards $Co(OH)_2$) interfacial band bending, i.e., electric field, after Fermi level alignment. Such interfacial band bending is expected to help charge separation in the composite by driving the photogenerated e^- towards $Co(OH)_2$ and h^+ towards Co_3O_4.

The (photo)electrochemical properties of the materials were studied by transient photocurrent measurements and electrochemical impedance spectroscopy (EIS) (Fig. 3a,b). The photocurrent curves in Fig. 3a give insights into the charge separation ability of the materials. Upon illumination the Co_3O_4@$Co(OH)_2$ reaches a photocurrent density of 0.09 μA/cm^2, higher than those of Co_3O_4 and $Co(OH)_2$, 0.07 and 0.03 μA/cm^2, respectively. Overall, the decay in the photocurrent curve is definitely diminished in the case of the composite, showing the enhanced charge separation of the e^--h^+ pairs in the case of Co_3O_4@$Co(OH)_2$. In addition, EIS in Fig. 3b allows to visualize another relevant feature of the composite, i.e., the resistance of the material. The fitted curve radius of Co_3O_4@$Co(OH)_2$ is the smallest among all the three cobalt compounds which means that Co_3O_4@$Co(OH)_2$ has the lowest

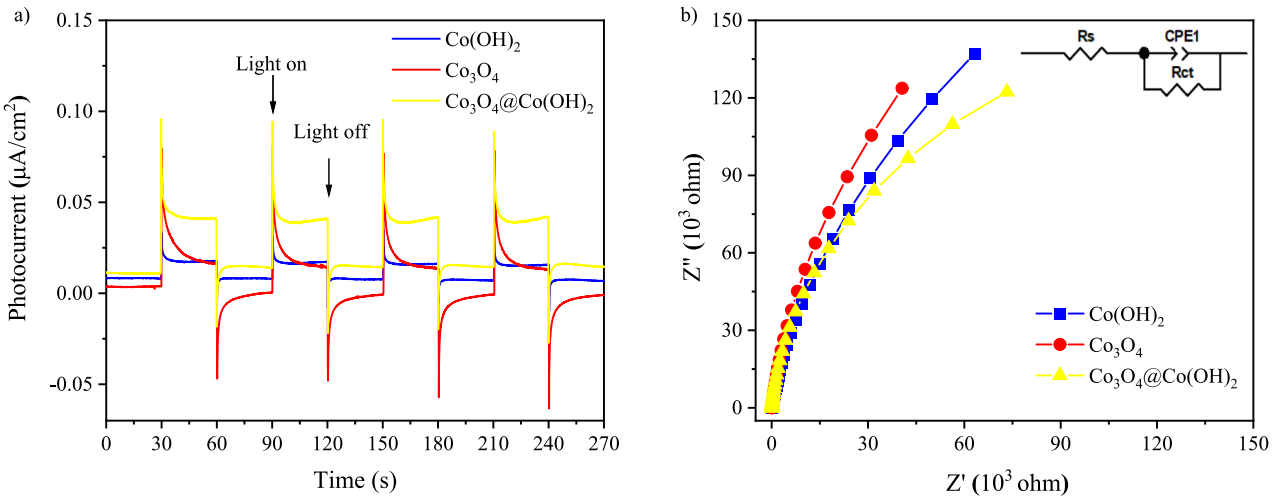

Fig. 3. (a) Chopped-light photocurrent responses and (b) EIS of Co_3O_4@$Co(OH)_2$, Co_3O_4 and $Co(OH)_2$.

resistance for charge transfer, referred as R_{ct} in the inset equivalent electric circuit model shown in Fig. 3b. R_{ct} was calculated to $3.2 \times 10^5 \Omega/cm^2$ for the heterostructure while the values for the oxide or hydroxide could not be obtained for the rather large radius. Furthermore, the semicircles are not available in the current EIS measurements, as commonly observer in other impedance spectroscopic studies of photocatalysts [78,79]. Taking into account all the above-mentioned characterization of the composite, the synthesized Co_3O_4@$Co(OH)_2$ presents superior properties for photocatalytic activity compared to its pure Co_3O_4 and $Co(OH)_2$ components.

3.3. Photocatalytic activity of Co_3O_4@$Co(OH)_2$ and mechanism

3.3.1. Photocatalytic activity

The photocatalytic degradation of MPs in water under white-light LED using the heterostructure Co_3O_4@$Co(OH)_2$ was evaluated and compared with those of the pure components, Co_3O_4 and $Co(OH)_2$. The weight loss (WL) of the MPs collected in a microporous membrane (see SI) was first considered. Co_3O_4@$Co(OH)_2$ achieved a MPs WL% of 40%, higher than previous reports with different photocatalysts such as TiO_2 [80,81] and pure Co_3O_4 and $Co(OH)_2$ with WL% of 25% and 12%, respectively.

The photocatalytic degradation of the polymer was also evaluated by SEM, i.e., by analyzing the changes in morphology and size of the MPs. As shown in Fig. 4, the morphology of the MPs changes quite drastically from spherical shapes to irregular ones upon photocatalytic degradation in presence of Co_3O_4@$Co(OH)_2$, but the spherical shape is kept upon using Co_3O_4 and $Co(OH)_2$. The changes in morphology are also reflected in the measured diameters. The MPs diameter distribution gets smaller and broader upon using Co_3O_4@$Co(OH)_2$: its center decreases from 0.91 to 0.81 μm and the full width at half-maximum increases from 0.05 to 0.46 μm (Fig. 4). However, Co_3O_4 and $Co(OH)_2$ do not affect much the MPs diameter distribution, only Co_3O_4 slightly decreases it to 0.83 μm. Comparing the distribution of the MPs on silicon wafer at small magnification (Fig. S11), the lower amount of particles is noticeable in the case of Co_3O_4@$Co(OH)_2$, in great accordance with the higher weight loss obtained in this case. By comparing the samples obtained after 3 days and 9 days of reaction, Fig. S11 also shows a decreased amount of MPs upon photocatalytic process, especially pronounced in the case of Co_3O_4@$Co(OH)_2$. Control experiments were conducted in order to confirm the relevance of both the photocatalyst and the light source. Indeed, the morphology and size of the MPs were not changed in the controlled experiment where the suspension of Co_3O_4@$Co(OH)_2$ and MPs was kept in dark (Fig. S12). Additionally, they were not affected by photolysis in absence of the heterostructure (Fig. S12).

Samples obtained at shorter reaction times allow to understand the higher activity of the composite, compared to the pure components. After 3 days the catalyst Co_3O_4@$Co(OH)_2$ covers almost completely the MPs, while Co_3O_4 and $Co(OH)_2$ are more dispersed (Fig. S13), which might be related to the higher activity of the composite in the degradation. In addition, energy dispersive X-ray (EDX) mapping and point analysis show the increase of oxygen in the MPs after degradation, as shown in Fig. S14. The presence of O cannot only be explained by the proximity of Co-oxygenated species, but indicates the formation of new oxygenated groups on the surface of the MPs, demonstrating the success of the oxidative processes at the MPs [9,82]. The morphological determinations of the MPs infers that the photocatalytic removal of MPs undergoes several stages. First, Co_3O_4@$Co(OH)_2$ was attached to the MPs, as visibly seen in the SEM images in Fig. S13. Under the light irradiation and in presence of the heterostructure, the MPs were photodegraded, leading to a coarse surface as seen in Fig. 4. The attachment of the composite on the MPs is in favor of a continuous degradation process, as the incident light absorbed by the composite will create radicals [83]. Over the photocatalysis time, part of MPs is removed, leading to a smaller average size but with a broader distribution (Fig. 4d). The change of the morphology is in line with the degradation rates. A larger morphologic difference between MPs before and after photocatalysis refers to a higher degradation rate, with the Co_3O_4@$Co(OH)_2$ topping at 40 wt%. To further confirm the degradation of the MPs, LC-MS analysis was performed and, despite the very low concentration, a molecule with $m/z = 167$ was identified, as shown in Fig. S15. This small fragment might come from the degradation of the 1,4-diphenyl-2-butanol, which represents a common product obtained from the degradation of PS [84]. To prove that also solar light could degrade the MPs, we also performed an experiment with a solar simulator, which brought to the degradation of MPs as shown in Fig. S16.

By preparing a suspension of Co_3O_4@$Co(OH)_2$ (8 mg) in water, it was possible to observe hydrogen evolution upon white-light LED irradiation (Fig. S17), with a H_2 production of 43 μmol g^{-1}. An AQE of 3.48% for H_2 evolution was calculated at a wavelength of 420 nm, and this decreased for larger wavelengths following the light absorbance of the composite (Fig. 5). On the other hand, the isolated compounds Co_3O_4 and $Co(OH)_2$ did not show any activity towards generation of H_2. Photocatalytic test of simultaneous MPs degradation and hydrogen evolution was also performed. Despite observation of MPs degradation, no H_2 could be detected.

Recyclability tests were also performed. Due to the attachment onto the MPs as shown in Fig. S11, the cobalt composite cannot be recycled after photocatalysis. Thus, the recyclability was only tested for hydrogen evolution (Fig. S18), showing similar activity in the second cycle and

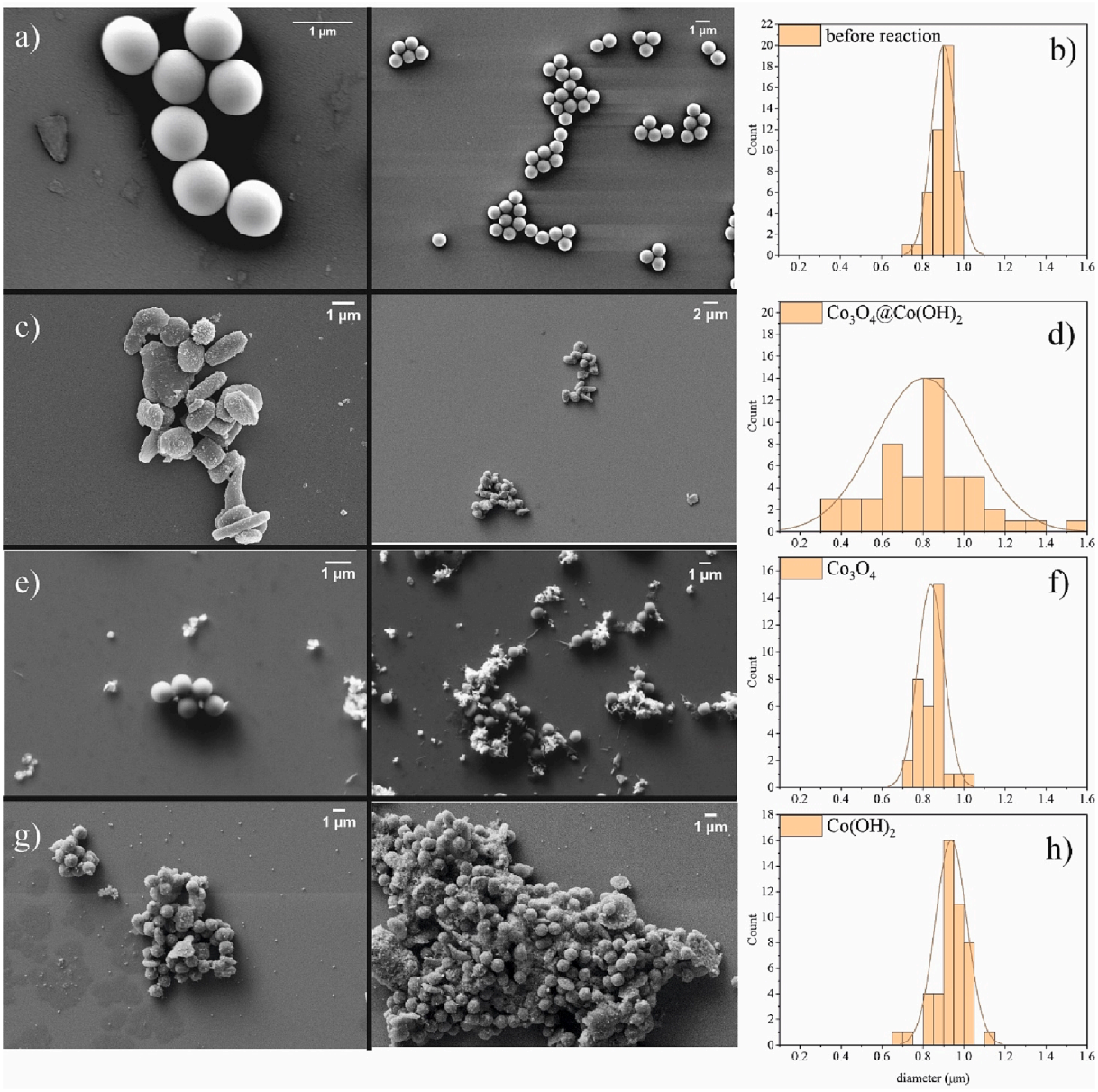

Fig. 4. SEM images of MPs before degradation (a) and after photodegradation using Co_3O_4@$Co(OH)_2$ (c), Co_3O_4 (e) and $Co(OH)_2$ (g) and the corresponding size distributions (b, d, f, h).

only a decrease of activity in the third cycle (Fig. S19). We further performed leaching test of Co via inductively coupled plasma optical emission spectroscopy (ICP-OES). A value of 4 mg L^{-1} was obtained, which represents the 1.25% of the Co in the reaction. The rather small leaching amount is in accordance with Co-based catalysts used in aqueous conditions [85], and might be attributed to the error of the centrifugation procedure for the removal of the solid catalyst after reaction.

3.3.2. *DFT studies*

The composite Co_3O_4@$Co(OH)_2$ was constructed using a cubic normal spinel structure Co_3O_4 crystal and a hexagonal layered hydroxide β–$Co(OH)_2$ crystal, as shown in Fig. 6. The conventional unit cell parameters for pristine Co_3O_4 and $Co(OH)_2$ were optimized first and found to belong to the F_{d3m} and P_{3m1} space groups, respectively, in agreement with the XRD patterns. The lattice constants were calculated to a = b = c = 8.359 Å, α = β = γ = 90° for the cubic Co_3O_4, and a = b = 3.187 Å, c = 4.736 Å, α = β = 90°, γ = 120° for the $Co(OH)_2$, respectively. Estimated lattice constants are slightly larger than the experimental results, which is typical of the generalized gradient approximation (GGA) functional [66,86–89].

The composites formed by $Co(OH)_2$ (0 0 1) and Co_3O_4 (1 1 1) planes were built based on the results given by the HR-TEM. Both $Co(OH)_2$ (0 0 1) and Co_3O_4 (1 1 1) layers show the same hexagonal phase, making the later alignment stages easier. Over 20 initial Co_3O_4@$Co(OH)_2$ composites with interfaces composed of different types of atomic layers were built for further optimization since both Co_3O_4 and $Co(OH)_2$ crystals are composed of anisotropic structures. All atoms were fully relaxed during the geometric optimization.

Fig. 6 illustrates the most stable structure of Co_3O_4@$Co(OH)_2$ composite standing out from other candidates. The whole composite contains 164 atoms including 32 H atoms, 80 O atoms, and 52 Co atoms. The xy-plane lattice constant of the heterojunction is a = b = 6.165 Å. The interface of the heterojunction is closely bonded with each other through the O surface of Co_3O_4 and Co surface of $Co(OH)_2$. The average bond lengths of Co-O at the interface is 2.04 Å, between the Co-O bond

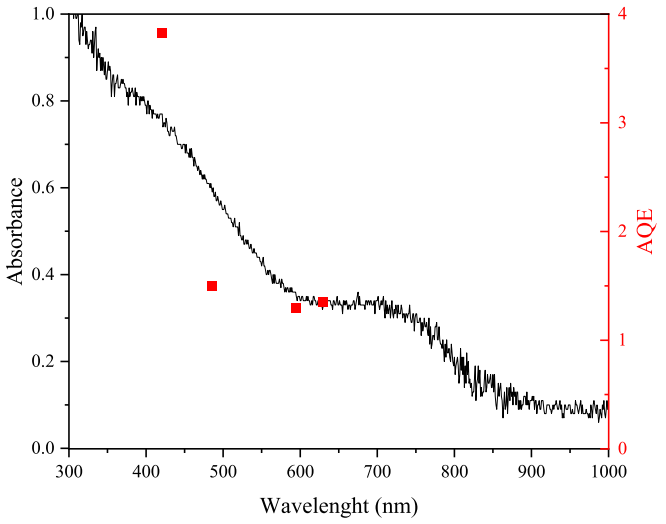

Fig. 5. Absorbance (black curve) and AQE (red dots) obtained for H_2 evolution at 420 nm, 485 nm, 595 nm and 630 nm using Co_3O_4@$Co(OH)_2$ in water and white-light LED irradiation. (For interpretation of the references to color in this figure legend, the reader is referred to the web version of this article.)

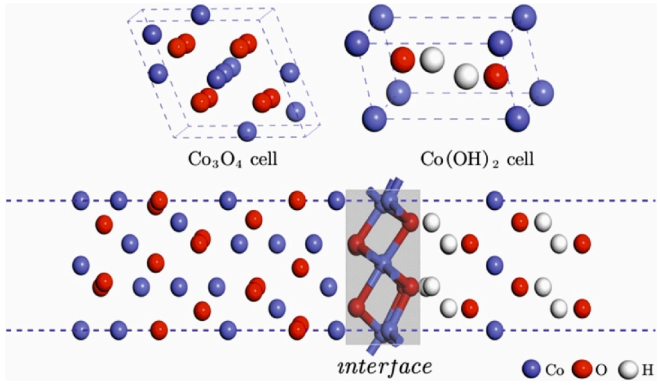

Fig. 6. Optimized crystal structures of the pristine $Co(OH)_2$ and Co_3O_4, and of the Co_3O_4@$Co(OH)_2$ heterojunction. The gray color represents the interface.

length of the pure Co_3O_4 with 1.98 Å and the $Co(OH)_2$ with 2.10 Å. The strong interactions at the interface obtained from DFT calculations verify the successful experimental synthesis of the heterojunction with XRD and SEM analysis.

Moreover, Fig. S20 suggests that the CB of Co_3O_4 is the original location in the heterostructure for the electrons after irradiation. While the negative-charged carriers will move through the interface to the CB of $Co(OH)_2$, the h^+ will accumulate at the VB of Co_3O_4. These phenomena will allow the charge separation and favor the photocatalytic reaction, in good agreement with the experimental results (see Section 3.2), which suggested the same pathway for the photogeneration of charge carriers.

3.3.3. *Proposed mechanism*

Upon irradiation, an e^--h^+ pair will be generated, and in the heterostructure charge carriers will migrate to the hetero-sites of proper energy levels where reduction and oxidation will happen. In the system herein studied, the energy level measurements and DFT revealed the presence of an interfacial electric field which helps charge carrier separation, i.e., e^- at the CB of $Co(OH)_2$ and h^+ at the VB of Co_3O_4, as in a type-II heterojunction [90]. These findings suggest that the reduction will happen on the $Co(OH)_2$ and the oxidation on the Co_3O_4. Herein we propose energy band diagrams after contact between the two semiconductors composing the heterostructure (Fig. 7a) and mechanisms for the photocatalytic MPs degradation and H_2 evolution (Fig. 7b and c).

Fig. 7b shows the proposed MPs degradation mechanism. Advanced oxidation processes (AOPs) are well-known as the basis for the degradation of organic molecules by forming radical oxygen species (ROS), such as OH• and $O_2^{\bullet -}$, which can attack the molecules and break the covalent bonds by cascade oxidative processes [91]. In the case of the MPs, the radicals can cause the oxidative cleavage of the long polymeric chain forming the MPs and generate smaller molecules, identifiable by LC-MS. When using the Co_3O_4@$Co(OH)_2$ composite, the superoxide radical $O_2^{\bullet -}$ can be theoretically generated from the reduction of O_2 at the E_c of $Co(OH)_2$. Indeed, the formation of the superoxide was verified by electron paramagnetic resonance (EPR) experiments in Fig. S21, which shows an increase of the DMPO- $O_2^{\bullet -}$ adduct by increasing the irradiation time. Surprisingly, also the hydroxyl radical OH• was detected by EPR, despite the shallow E_v of Co_3O_4, which would make thermodynamically impossible the formation of the hydroxyl radical [92]. Consequently, the only possible pathway for the formation of this radical is *via* the reaction of the superoxide with the protons in solution [93], as shown in Fig. 7b. To further demonstrate the relevance of AOPs, radical scavengers were added to the suspension to verify the absence of degradation when the radicals are quenched. K_2CrO_4/Ar and i-PrOH were used to quench $O_2^{\bullet -}$ and OH•, respectively [94]. As shown in Fig. S22, the MPs were preserved when using both the radical scavengers, suggesting that $O_2^{\bullet -}$ and OH• are both involved in the degradation, as demonstrated by EPR measurements. Finally, Fig. 7c depicts the H_2 formation favored by the presence of the Co_3O_4@$Co(OH)_2$ composite. The photogenerated e^- migrate to the E_c of $Co(OH)_2$ and consequently allow the water reduction to H_2.

The two reduction reactions $O_2/O_2^{\bullet -}$ and H^+/H_2 can happen simultaneously in both processes studied in this work, i.e., MPs degradation and H_2 production. Nevertheless, the former is performed without purging the system and this will favor the formation of $O_2^{\bullet -}$ due to a higher concentration of O_2 in the reaction vessel. On the other hand,

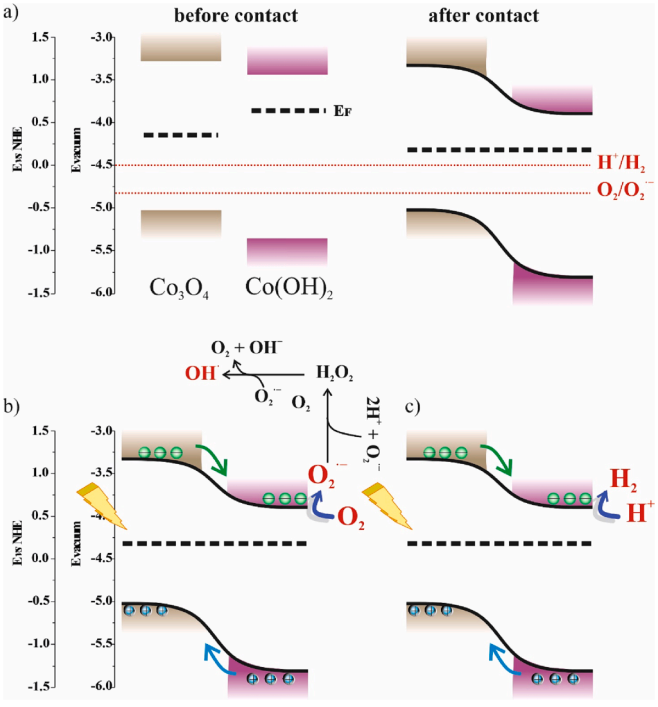

Fig. 7. (a) Energy band diagrams of Co_3O_4 and $Co(OH)_2$ before and after the contact. (b) Proposed mechanism of the formation of radicals involved in the MPs degradation and (c) for the hydrogen evolution reaction promoted by the Co_3O_4@$Co(OH)_2$ composite.

the H_2 production reaction was performed after purging the system with argon, which led to a negligible amount O_2 as confirmed by GC. In this case, the purging procedure ensures a reliable hydrogen quantification and avoids the reduction of O_2 to $O_2^{\bullet -}$. Thus, Co_3O_4@$Co(OH)_2$ will improve the formation of radicals in the case of degradation reaction and will increase the H_2 evolution by decreasing the recombination rate compared to the pure components of the composite. Indeed, the pure components would not benefit from the separation of charge carriers, as confirmed by photocurrent measurement, then eventual recombination would happen, and the reactions described in this work would be unlikely to occur.

Functionalities and performances of the present photocatalytic heterostructures are compared with the recent works based on cobalt oxides and hydroxides, as tabulated in Table S3. From the Table, the cobalt oxides and hydroxides have been proven as active catalysts with vast applications individually in hydrogen evolution or organic dye removals or combinations of both. Our current result supports the reported works, and moreover, displays two unique features under visible light irradiation: the removal of persistent MPs and the hydrogen evolution without any scavenger. These features make the Co_3O_4@$Co(OH)_2$ advantageous in practical photocatalytic applications.

4. Conclusions

This work demonstrates the suitability of one-pot synthesis of Co_3O_4@$Co(OH)_2$ semiconductor composites, following a hydrothermal synthesis under controlled pH conditions. The characterization of the composite demonstrated that the intimate contact between the two components of the material positively influenced its photocatalytic ability. Indeed, photocurrent measurement demonstrated the increase in charge separation in the composite, compared to the pure components, and XAS analysis demonstrated a stabilization of $Co(OH)_2$ in the composite rather than as a pure compound. These improved characteristics allowed its photocatalytic activity, demonstrated in PS MPs degradation and hydrogen evolution reaction. In both cases the pure components, Co_3O_4 and $Co(OH)_2$, did not show any activity for the reactions of interest, due to photoinduced-charge recombination. This Co_3O_4@$Co(OH)_2$ photocatalyst provides new avenues for the application of semiconductor composites in the photocatalytic degradation of MPs, as well as for its use in hydrogen evolution. Combining its suitability in MPs removal and hydrogen production, it might represent a good starting point for the photoreforming of MPs, upon modification of the catalyst. Moreover, the materials activation routes and mechanistic studies down to electronic structural level knowledge are hoped to inspire and rationalize facile preparations and functionalization of active photocatalysts combining the hydroxide and oxide of the same metal.

CRediT authorship contribution statement

Rossella Greco: Conceptualization, Data curation, Methodology, Validation, Investigation, Writing – original draft. **Lucía Baxauli-Marin:** Investigation, Validation. **Filipp Temerov:** Writing – review & editing. **Matyas Daboczi:** Investigation, Data curation, Writing – review & editing. **Salvador Eslava:** Writing – review & editing. **Yuran Niu:** Data curation. **Alexei Zakharov:** Investigation. **Meng Zhang:** Investigation, Writing – review & editing. **Taohai Li:** Investigation, Writing – review & editing. **Wei Cao:** Conceptualization, Writing – review & editing, Supervision, Funding acquisition.

Declaration of Competing Interest

The authors declare that they have no known competing financial interests or personal relationships that could have appeared to influence the work reported in this paper.

Data availability

All data generated or analyzed during this study are included in this published article (and its supplementary information files).

Acknowledgements

R.G., F.T., and W.C. acknowledge financial support from the European Research Council (ERC) under the European Union's Horizon 2020 research and innovation programme (grant agreement No. 101002219). S.E. and M.D. acknowledge the EPSRC grant EP/S030727/1 for financial support. Authors gratefully acknowledge the Center of Materials Analysis (CMA), University of Oulu and Biocenter, University of Oulu, for the characterization techniques and LC-MS analysis. R.G. acknowledges Javier Fernández-Catalá and Romain Botella for the useful discussions during the sample optimization. We acknowledge MAX IV Laboratory for time on Beamline [MAXPEEM] under Proposal [20210172]. Research conducted at MAX IV, a Swedish national user facility, is supported by the Swedish Research council under contract 2018-07152, the Swedish Governmental Agency for Innovation Systems under contract 2018-04969, and Formas under contract 2019-02496.

Appendix A. Supplementary data

Supplementary data to this article can be found online at https://doi.org/10.1016/j.cej.2023.144569.

References

[1] H. Hou, X. Zhang, Rational design of 1D/2D heterostructured photocatalyst for energy and environmental applications, Chem. Eng. J. 395 (2020), 125030, https://doi.org/10.1016/j.cej.2020.125030.
[2] Y. Zhao, S. Zhang, R. Shi, G.I.N. Waterhouse, J. Tang, T. Zhang, Two-dimensional photocatalyst design: a critical review of recent experimental and computational advances, Mater. Today. 34 (2020) 78–91, https://doi.org/10.1016/j.mattod.2019.10.022.
[3] L. Liu, M. Xu, Y. Ye, B. Zhang, On the degradation of (micro)plastics: degradation methods, influencing factors, environmental impacts, Sci. Total Environ. 806 (2022), 151312, https://doi.org/10.1016/J.SCITOTENV.2021.151312.
[4] R.C. Thompson, Y. Olson, R.P. Mitchell, A. Davis, S.J. Rowland, A.W.G. John, D. McGonigle, A.E. Russell, Lost at sea: Where Is All the Plastic?, Science (80-.). 304 (2004) 838. https://doi.org/10.1126/SCIENCE.1094559/SUPPL_FILE/THOMPSON.SOM.PDF.
[5] O. Pereao, B. Opeolu, O. Fatoki, Microplastics in aquatic environment: characterization, ecotoxicological effect, implications for ecosystems and developments in South Africa, Environ. Sci. Pollut. Res. 27 (2020) 22271–22291, https://doi.org/10.1007/s11356-020-08688-2.
[6] A. Wegner, E. Besseling, E.M. Foekema, P. Kamermans, A.A. Koelmans, Effects of nanopolystyrene on the feeding behavior of the blue mussel (Mytilus edulis L.), Environ. Toxicol. Chem. 31 (2012) 2490–2497, https://doi.org/10.1002/etc.1984.
[7] Z. Ouyang, Y. Yang, C. Zhang, S. Zhu, L. Qin, W. Wang, D. He, Y. Zhou, H. Luo, F. Qin, Recent advances in photocatalytic degradation of plastics and plastic-derived chemicals, J. Mater. Chem. A. 9 (2021) 13402–13441, https://doi.org/10.1039/D0TA12465F.
[8] C. Xing, G. Yu, J. Zhou, Q. Liu, T. Chen, H. Liu, X. Li, Solar energy-driven upcycling of plastic waste on direct Z-scheme heterostructure of V-substituted phosphomolybdic acid/g-C3N4 nanosheets, Appl. Catal. B Environ. 315 (2022), 121496, https://doi.org/10.1016/J.APCATB.2022.121496.
[9] R. Jiang, G. Lu, Z. Yan, J. Liu, D. Wu, Y. Wang, Microplastic degradation by hydroxy-rich bismuth oxychloride, J. Hazard. Mater. 405 (2021), 124247, https://doi.org/10.1016/j.jhazmat.2020.124247.
[10] A. Uheida, H.G. Mejía, M. Abdel-Rehim, W. Hamd, J. Dutta, Visible light photocatalytic degradation of polypropylene microplastics in a continuous water flow system, J. Hazard. Mater. 406 (2021), 124299, https://doi.org/10.1016/J.JHAZMAT.2020.124299.
[11] S. Kim, A. Sin, H. Nam, Y. Park, H. Lee, C. Han, Advanced oxidation processes for microplastics degradation: a recent trend, Chem. Eng. J. Adv. 9 (2022), 100213, https://doi.org/10.1016/J.CEJA.2021.100213.
[12] M.H. Fadli, M. Ibadurrohman, S. Slamet, Microplastic pollutant degradation in water using modified tio photocatalyst under uv-irradiation, IOP Conf. Ser. Mater. Sci. Eng. 1011 (2021), https://doi.org/10.1088/1757-899X/1011/1/012055.
[13] S.Y. Tan, W.C. Chong, S. Sethupathi, Y.L. Pang, L.C. Sim, E. Mahmoudi, Optimisation of aqueous phase low density polyethylene degradation by graphene oxide-zinc oxide photocatalysts, Chem. Eng. Res. Des. 190 (2023) 550–565, https://doi.org/10.1016/j.cherd.2022.12.045.

[14] K.S. Novoselov, A. Mishchenko, A. Carvalho, A.H. Castro Neto, 2D materials and van der Waals heterostructures, Science 80 (2016) 353, https://doi.org/10.1126/science.aac9439.

[15] J. Low, S. Cao, J. Yu, S. Wageh, Two-dimensional layered composite photocatalysts, Chem. Commun. 50 (2014) 10768, https://doi.org/10.1039/C4CC02553A.

[16] W. Ou, Y. Xu, H. Zhou, C. Su, Harnessing photoexcited redox centers of semiconductor photocatalysts for advanced synthetic chemistry, Sol. RRL. 5 (2) (2021) 2000444.

[17] J. Liqiang, Q. Yichun, W. Baiqi, L. Shudan, J. Baojiang, Y. Libin, F. Wei, F. Honggang, S. Jiazhong, Review of photoluminescence performance of nano-sized semiconductor materials and its relationships with photocatalytic activity, Sol. Energy Mater. Sol. Cells. 90 (2006) 1773–1787, https://doi.org/10.1016/j.solmat.2005.11.007.

[18] C. Yuan, X. Zhang, L. Hou, L. Shen, D. Li, F. Zhang, C. Fan, J. Li, Lysine -assisted hydrothermal synthesis of urchin-like ordered arrays of mesoporous Co(OH)2 nanowires and their application in electrochemical capacitors, J. Mater. Chem. 20 (2010) 10809–10816, https://doi.org/10.1039/C0JM02174A.

[19] D. Wang, Q. Wang, T. Wang, Morphology-controllable synthesis of cobalt oxalates and their conversion to mesoporous Co3O4 nanostructures for application in supercapacitors, Inorg. Chem. 50 (2011) 6482–6492, https://doi.org/10.1021/IC200309T/SUPPL_FILE/IC200309T_SI_001.PDF.

[20] F. Manteghi, S.H. Kazemi, M. Peyvandipour, A. Asghari, Preparation and application of cobalt oxide nanostructures as electrode materials for electrochemical supercapacitors, RSC Adv. 5 (2015) 76458–76463, https://doi.org/10.1039/C5RA09060A.

[21] A.R. Kamali, D. Qiao, Z. Shi, D. Wang, Green molten salt modification of cobalt oxide for lithium ion battery anode application, Mater. Chem. Phys. 267 (2021), 124585, https://doi.org/10.1016/J.MATCHEMPHYS.2021.124585.

[22] A.P. Tiwari, S.H. Chae, G.P. Ojha, B. Dahal, T. Mukhiya, M. Lee, K. Chhetri, T. Kim, H.Y. Kim, Three-dimensional porous carbonaceous network with in-situ entrapped metallic cobalt for supercapacitor application, J. Colloid Interface Sci. 553 (2019) 622–630, https://doi.org/10.1016/J.JCIS.2019.06.070.

[23] B.W. Qin, K.C. Huang, Y. Zhang, L. Zhou, Z. Cui, K. Zhang, X.Y. Zhang, J.P. Zhang, Diverse structures based on a heptanuclear cobalt cluster with 0d to 3d metal-organic frameworks: magnetism and application in batteries, Chem. – A Eur. J. 24 (2018) 1962–1970, https://doi.org/10.1002/CHEM.201705023.

[24] H.Z. Wan, J.J. Jiang, J.W. Yu, Y.J. Ruan, L. Peng, L. Zhang, H.C. Chen, S.W. Bie, Cobalt sulfide nanotube arrays grown on FTO and graphene membranes for high-performance supercapacitor application, Appl. Surf. Sci. 311 (2014) 793–798, https://doi.org/10.1016/J.APSUSC.2014.05.169.

[25] Y. Mussa, F. Ahmed, H. Abuhimd, M. Arsalan, E. Alsharaeh, Enhanced electrochemical performance at high temperature of cobalt oxide/reduced graphene oxide nanocomposites and its application in lithium-ion batteries, Sci Rep 9 (1) (2019) 1–10, https://doi.org/10.1038/s41598-018-37032-5.

[26] P. Gao, Y. Zeng, P. Tang, Z. Wang, J. Yang, A. Hu, J. Liu, P. Gao, Y. Zeng, P. Tang, Z. Wang, A. Hu, J. Liu, J. Yang, Understanding the synergistic effects and structural evolution of co(oh)2 and co3o4 toward boosting electrochemical charge storage, Adv. Funct. Mater. 32 (2022) 2108644, https://doi.org/10.1002/ADFM.202108644.

[27] R. Mei, U. Dhawa, R.C. Samanta, W. Ma, J. Wencel-Delord, L. Ackermann, Cobalt-catalyzed oxidative c−h activation: strategies and concepts, ChemSusChem. 13 (2020) 3306–3356, https://doi.org/10.1002/CSSC.202000024.

[28] S. Hatamie, M.M. Ahadian, A. Rashidi, A. Karimi, O. Akhavan, Novel synthesis of cobalt/poly vinyl alcohol/gamma alumina nanocomposite for catalytic application, Appl. Phys. A Mater. Sci. Process. 123 (2017) 1–10, https://doi.org/10.1007/S00339-017-0913-6/FIGURES/8.

[29] T. Kobayashi, H. Yorimitsu, K. Oshima, Cobalt-catalyzed isomerization of 1-alkenes to (e)-2-alkenes with dimethylphenylsilylmethylmagnesium chloride and its application to the stereoselective synthesis of (e)-alkenylsilanes, Chem. – An Asian J. 4 (2009) 1078–1083, https://doi.org/10.1002/ASIA.200900111.

[30] H. Ohmiya, K. Wakabayashi, H. Yorimitsu, K. Oshima, Cobalt-catalyzed cross-coupling reactions of alkyl halides with aryl Grignard reagents and their application to sequential radical cyclization/cross-coupling reactions, Tetrahedron. 62 (2006) 2207–2213, https://doi.org/10.1016/J.TET.2005.12.013.

[31] H. Someya, H. Ohmiya, H. Yorimitsu, K. Oshima, Cobalt-catalyzed sequential cyclization/cross-coupling reactions of 6-halo-1-hexene derivatives with Grignard reagents and their application to the synthesis of 1,3-diols, Tetrahedron. 63 (2007) 8609–8618, https://doi.org/10.1016/J.TET.2007.04.083.

[32] H. Ohmiya, H. Yorimitsu, K. Oshima, Cobalt(diamine)-catalyzed cross-coupling reaction of alkyl halides with arylmagnesium reagents: stereoselective constructions of arylated asymmetric carbons and application to total synthesis of AH13205, J. Am. Chem. Soc. 128 (2006) 1886–1889, https://doi.org/10.1021/JA057560O/SUPPL_FILE/JA057560OSI20051212_090326.PDF.

[33] G. Pototschnig, N. Maulide, M. Schnürch, Direct functionalization of c−h bonds by iron, nickel, and cobalt catalysis, Chem. – A Eur. J. 23 (2017) 9206–9232, https://doi.org/10.1002/CHEM.201605657.

[34] J.J. Bozell, B.R. Haines, D.R. Dimmel, Cobalt-Schiff base complex catalyzed oxidation of para-substituted phenolics. preparation of benzoquinones, accessed January 13, 2022, J. Org. Chem. 60 (1995) 2398–2404, https://pubs.acs.org/sharingguidelines.

[35] P.G. Harrison, I.K. Ball, W. Daniell, P. Lukinskas, M. Céspedes, E.E. Miró, M.A. Ulla, Cobalt catalysts for the oxidation of diesel soot particulate, Chem. Eng. J. 95 (2003) 47–55, https://doi.org/10.1016/S1385-8947(03)00077-9.

[36] J.B. McManus, J.D. Griffin, A.R. White, D.A. Nicewicz, Homobenzylic oxygenation enabled by dual organic photoredox and cobalt catalysis, J. Am. Chem. Soc. 142 (2020) 10325–10330, https://doi.org/10.1021/JACS.0C04422/SUPPL_FILE/JA0C04422_SI_001.PDF.

[37] S. Zafeiratos, T. Dintzer, D. Teschner, R. Blume, M. Hävecker, A. Knop-Gericke, R. Schlögl, Methanol oxidation over model cobalt catalysts: influence of the cobalt oxidation state on the reactivity, J. Catal. 269 (2010) 309–317, https://doi.org/10.1016/J.JCAT.2009.11.013.

[38] H.K. Lin, H.C. Chiu, H.C. Tsai, S.H. Chien, C. Bin Wang, Synthesis, Characterization and Catalytic Oxidation of Carbon Monoxide over Cobalt Oxide, Catal. Lett. 2003 883. 88 (2003) 169–174. https://doi.org/10.1023/A:1024013822986.

[39] B. Solsona, T.E. Davies, T. Garcia, I. Vázquez, A. Dejoz, S.H. Taylor, Total oxidation of propane using nanocrystalline cobalt oxide and supported cobalt oxide catalysts, Appl. Catal. B Environ. 84 (2008) 176–184, https://doi.org/10.1016/J.APCATB.2008.03.021.

[40] P. Hu, M. Long, Cobalt-catalyzed sulfate radical-based advanced oxidation: a review on heterogeneous catalysts and applications, Appl. Catal. B Environ. 181 (2016) 103–117, https://doi.org/10.1016/J.APCATB.2015.07.024.

[41] J. Lan, D. Qi, J. Song, P. Liu, Y. Liu, Y.X. Pan, Noble-metal-free cobalt hydroxide nanosheets for efficient electrocatalytic oxidation, Front. Chem. Sci. Eng. 14 (2020) 948–955, https://doi.org/10.1007/S11705-020-1920-2.

[42] M. Vidotti, M.R. Silva, R.P. Salvador, S.I.C. de Torresi, L.H. Dall'Antonia, Electrocatalytic oxidation of urea by nanostructured nickel/cobalt hydroxide electrodes, Electrochim. Acta. 53 (2008) 4030–4034, https://doi.org/10.1016/J.ELECTACTA.2007.11.029.

[43] M. Jafarian, M.G. Mahjani, H. Heli, F. Gobal, H. Khajehsharifi, M.H. Hamedi, A study of the electro-catalytic oxidation of methanol on a cobalt hydroxide modified glassy carbon electrode, Electrochim. Acta. 48 (2003) 3423–3429, https://doi.org/10.1016/S0013-4686(03)00399-2.

[44] V. Artero, M. Chavarot-Kerlidou, M. Fontecave, V. Artero, M. Fontecave, M. Chavarot-Kerlidou, Splitting water with cobalt, Angew. Chemie Int. Ed. 50 (2011) 7238–7266, https://doi.org/10.1002/ANIE.201007987.

[45] E.S. Andreiadis, P.-A. Jacques, P.D. Tran, A. Leyris, M. Chavarot-Kerlidou, B. Jousselme, M. Matheron, J. Pécaut, S. Palacin, M. Fontecave, V. Artero, Molecular engineering of a cobalt-based electrocatalytic nanomaterial for H2 evolution under fully aqueous conditions, Nat. Chem. 5 (1) (2013) 48–53.

[46] S. Kumaravel, P. Thiruvengetam, S.R. Ede, K. Karthick, S. Anantharaj, S. Sam Sankar, S. Kundu, Cobalt tungsten oxide hydroxide hydrate (CTOHH) on DNA scaffold: an excellent bi-functional catalyst for oxygen evolution reaction (OER) and aromatic alcohol oxidation, Dalt, Trans. 48 (2019) 17117–17131, https://doi.org/10.1039/c9dt03941d.

[47] M. Mathankumar, S. Anantharaj, A.K. Nandakumar, S. Kundu, B. Subramanian, Potentiostatic phase formation of β-CoOOH on pulsed laser deposited biphasic cobalt oxide thin film for enhanced oxygen evolution, J. Mater. Chem. A. 5 (2017) 23053–23066, https://doi.org/10.1039/c7ta07410g.

[48] R. Madhu, A. Karmakar, S. Kumaravel, S.S. Sankar, K. Bera, S. Nagappan, H. N. Dhandapani, S. Kundu, Revealing the pH-Universal electrocatalytic activity of co-doped RuO2toward the water oxidation reaction, ACS Appl. Mater. Interfaces. 14 (2022) 1077–1091, https://doi.org/10.1021/acsami.1c20752.

[49] S. Anantharaj, S.R. Ede, K. Sakthikumar, K. Karthick, S. Mishra, S. Kundu, Recent Trends and Perspectives in Electrochemical Water Splitting with an Emphasis on Sulfide, selenide, and phosphide catalysts of fe co, and ni: a review, ACS Catal. 6 (2016) 8069–8097, https://doi.org/10.1021/acscatal.6b02479.

[50] J. Del Pilar-Albaladejo, P.K. Dutta, Topotactic transformation of zeolite supported cobalt(II) hydroxide to oxide and comparison of photocatalytic oxygen evolution, ACS Catal. 4 (2014) 9–15, https://doi.org/10.1021/CS400991V/SUPPL_FILE/CS400991V_SI_001.PDF.

[51] J. Del-Pilar, B. Wang, P.K. Dutta, Anchoring of cobalt hydroxide catalysts on nanozeolite crystals for photocatalytic water oxidation, Microporous Mesoporous Mater. 217 (2015) 125–132, https://doi.org/10.1016/J.MICROMESO.2015.06.014.

[52] F. Zhang, A. Yamakata, K. Maeda, Y. Moriya, T. Takata, J. Kubota, K. Teshima, S. Oishi, K. Domen, Cobalt-modified porous single-crystalline LaTiO 2N for highly efficient water oxidation under visible light, J. Am. Chem. Soc. 134 (2012) 8348–8351, https://doi.org/10.1021/JA301726C/SUPPL_FILE/JA301726C_SI_001.PDF.

[53] K. Maeda, K. Teramura, D. Lu, N. Saito, Y. Inoue, K. Domen, Noble-metal/cr2o3 core/shell nanoparticles as a cocatalyst for photocatalytic overall water splitting, angew Chemie. 118 (2006) 7970–7973, https://doi.org/10.1002/ANGE.200602473.

[54] K. Maeda, K. Ishimaki, Y. Tokunaga, D. Lu, M. Eguchi, Modification of wide-band-gap oxide semiconductors with cobalt hydroxide nanoclusters for visible-light water oxidation, Angew Chemie. 128 (2016) 8449–8453, https://doi.org/10.1002/ANGE.201602764.

[55] A.K. Geim, I.V. Grigorieva, Van der Waals heterostructures, Nature 499 (7459) (2013) 419–425.

[56] Y. Zhan, G. Du, S. Yang, C. Xu, M. Lu, Z. Liu, J.Y. Lee, Development of cobalt hydroxide as a bifunctional catalyst for oxygen electrocatalysis in alkaline solution, ACS Appl. Mater. Interfaces. 7 (2015) 12930–12936, https://doi.org/10.1021/acsami.5b02670.

[57] L. Huang, J. Jiang, L. Ai, Interlayer expansion of layered cobalt hydroxide nanobelts to highly improve oxygen evolution electrocatalysis, ACS Appl. Mater. Interfaces. 9 (2017) 7059–7067, https://doi.org/10.1021/acsami.6b14479.

[58] J. Liu, J. Nai, T. You, P. An, J. Zhang, G. Ma, X. Niu, C. Liang, S. Yang, L. Guo, The flexibility of an amorphous cobalt hydroxide nanomaterial promotes the electrocatalysis of oxygen evolution reaction, Small. 14 (2018) 1703514, https://doi.org/10.1002/smll.201703514.

[59] G. Zhang, S. Zang, X. Wang, Layered Co(OH)<inf>2</inf> deposited polymeric carbon nitrides for photocatalytic water oxidation, ACS Catal. 5 (2015) 941–947, https://doi.org/10.1021/cs502002u.
[60] X. Ma, Y. Liu, Y. Wang, Z. Jin, Co3O4/CeO2 p-n heterojunction construction and application for efficient photocatalytic hydrogen evolution, Int. J. Hydrogen Energy. 46 (2021) 33809–33822, https://doi.org/10.1016/j.ijhydene.2021.07.201.
[61] S. Akshatha, S. Sreenivasa, L. Parashuram, V. Udaya kumar, F.A. Alharthi, T. M. Chakrapani Rao, S. kumar, Microwave assisted green synthesis of p-type Co3O4@Mesoporous carbon spheres for simultaneous degradation of dyes and photocatalytic hydrogen evolution reaction, Mater. Sci. Semicond. Process. 121 (2021), 105432, https://doi.org/10.1016/j.mssp.2020.105432.
[62] H. Pang, X. Li, Q. Zhao, H. Xue, W.Y. Lai, Z. Hu, W. Huang, One-pot synthesis of heterogeneous Co3O4-nanocube/Co(OH)2-nanosheet hybrids for high-performance flexible asymmetric all-solid-state supercapacitors, Nano Energy. 35 (2017) 138–145, https://doi.org/10.1016/J.NANOEN.2017.02.044.
[63] S. Farhadi, J. Safabakhsh, P. Zaringhadam, Synthesis, characterization, and investigation of optical and magnetic properties of cobalt oxide (Co3O4) nanoparticles, J Nanostruct Chem 3 (1) (2013).
[64] M. Wang, J.Q. Wang, C. Xi, C.Q. Cheng, C.Q. Zou, R. Zhang, Y.M. Xie, Z.L. Guo, C. C. Tang, C.K. Dong, Y.J. Chen, X.W. Du, A hydrogen-deficient nickel-cobalt double hydroxide for photocatalytic overall water splitting, Angew. Chemie - Int. Ed. 59 (2020) 11510–11515, https://doi.org/10.1002/ANIE.202002650.
[65] J. Feng, H.C. Zeng, Size-controlled growth of co3o4 nanocubes, Chem. Mater. 15 (2003) 2829–2835, https://doi.org/10.1021/CM020940D.
[66] R. Ma, K. Takada, K. Fukuda, N. Iyi, Y. Bando, T. Sasaki, Topochemical synthesis of monometallic (co2+–co3+) layered double hydroxide and its exfoliation into positively charged co(oh)2 nanosheets, Angew. Chemie Int. Ed. 47 (2008) 86–89, https://doi.org/10.1002/ANIE.200703941.
[67] X. Liu, G. Qiu, X. Li, Shape-controlled synthesis and properties of uniform spinel cobalt oxide nanocubes, Nanotechnology. 16 (12) (2005) 3035–3040.
[68] Y. Shen, Y. Jiang, Z. Yang, J. Dong, W. Yang, Q. An, L. Mai, Electronic structure modulation in moo2/mop heterostructure to induce fast electronic/ionic diffusion kinetics for lithium storage, Adv. Sci. 9 (2022) 2104504, https://doi.org/10.1002/ADVS.202104504.
[69] A.A. Malek Barmi, M. Aghazadeh, B. Arhami, H.M. Shiri, A.A. Fazl, E. Jangju, Porous cobalt hydroxide nanosheets with excellent supercapacitive behavior, Chem. Phys. Lett. 541 (2012) 65–69, https://doi.org/10.1016/J.CPLETT.2012.05.038.
[70] G. Cao, Y. Wang, Nanostructures and Nanomaterials, WORLD SCIENTIFIC, 2011.
[71] W. Cao, V. Pankratov, M. Huttula, X. Shi, S. Saukko, Z. Huang, M. Zhang, Gold nanoparticles on MoS2 layered crystal flakes, Mater. Chem. Phys. 158 (2015) 89–95, https://doi.org/10.1016/J.MATCHEMPHYS.2015.03.041.
[72] J. Yang, H. Liu, W.N. Martens, R.L. Frost, Synthesis and characterization of Cobalt hydroxide, cobalt oxyhydroxide, and cobalt oxide nanodiscs, J. Phys. Chem. C. 114 (2010) 111–119, https://doi.org/10.1021/JP908548F/SUPPL_FILE/JP908548F_SI_001.PDF.
[73] D.K. Bora, X. Cheng, M. Kapilashrami, P.A. Glans, Y. Luo, J.H. Guo, Influence of crystal structure, ligand environment and morphology on Co L-edge XAS spectral characteristics in cobalt compounds, J. Synchrotron Radiat. 22 (2015) 1450–1458, https://doi.org/10.1107/S1600577515017178/RV5036SUP1.PDF.
[74] S.A. Makhlouf, Z.H. Bakr, K.I. Aly, M.S. Moustafa, Structural, electrical and optical properties of Co3O4 nanoparticles, Superlattices Microstruct. 64 (2013) 107–117, https://doi.org/10.1016/J.SPMI.2013.09.023.
[75] I.D. Baikie, A.C. Grain, J. Sutherland, J. Law, Dual mode kelvin probe: featuring ambient pressure photoemission spectroscopy and contact potential difference, Energy Procedia. 60 (2014) 48–56, https://doi.org/10.1016/J.EGYPRO.2014.12.341.
[76] L. Qiao, W. Li, H. Xiao, H.M. Meyer, X. Liang, N.V. Nguyen, W.J. Weber, M. D. Biegalski, Electronic structure and band alignment at an epitaxial spinel/perovskite heterojunction, ACS Appl. Mater. Interfaces. 6 (2014) 14338–14344, https://doi.org/10.1021/am5036219.
[77] M. Suksomboon, K. Kongsawatvoragul, S. Duangdangchote, M. Sawangphruk, Reducing the energy band gap of cobalt hydroxide nanosheets with silver atoms and enhancing their electrical conductivity with silver nanoparticles, ACS Omega. 6 (2021) 20804–20811, https://doi.org/10.1021/ACSOMEGA.1C01908/ASSET/IMAGES/LARGE/AO1C01908_0006.JPEG.
[78] Y. Lei, K.H. Ng, Y. Zhu, Y. Zhang, Z. Li, S. Xu, J. Huang, J. Hu, Z. Chen, W. Cai, Y. Lai, Mo-activated VC as effective cocatalyst for an enhanced photocatalytic hydrogen evolution activity of CdS, Chem. Eng. J. 452 (2023), 139325, https://doi.org/10.1016/J.CEJ.2022.139325.
[79] Z. Hou, J. Yu, X. Zhou, Z. Chen, J. Xu, B. Zhao, W. Gen, H. Zhang, Enhanced performance of hybrid supercapacitors by the synergistic effect of Co(OH)2 nanosheets and NiMn layered hydroxides, J. Colloid Interface Sci. 646 (2023) 753–762, https://doi.org/10.1016/J.JCIS.2023.05.128.
[80] J. Shang, M. Chai, Y. Zhu, Solid-phase photocatalytic degradation of polystyrene plastic with TiO2 as photocatalyst, J. Solid State Chem. 174 (2003) 104–110, https://doi.org/10.1016/S0022-4596(03)00183-X.
[81] G.L. Liu, D.W. Zhu, S.J. Liao, L.Y. Ren, J.Z. Cui, W.B. Zhou, Solid-phase photocatalytic degradation of polyethylene–goethite composite film under UV-light irradiation, J. Hazard. Mater. 172 (2009) 1424–1429, https://doi.org/10.1016/J.JHAZMAT.2009.08.008.
[82] G. Liu, D. Zhu, W. Zhou, S. Liao, J. Cui, K. Wu, D. Hamilton, Solid-phase photocatalytic degradation of polystyrene plastic with goethite modified by boron under UV–vis light irradiation, Appl. Surf. Sci. 256 (2010) 2546–2551, https://doi.org/10.1016/J.APSUSC.2009.10.102.
[83] T.S. Tofa, K.L. Kunjali, S. Paul, J. Dutta, Visible light photocatalytic degradation of microplastic residues with zinc oxide nanorods, Environ. Chem. Lett. 17 (2019) 1341–1346, https://doi.org/10.1007/s10311-019-00859-z.
[84] H.M. Feng, J.C. Zheng, N.Y. Lei, L. Yu, K.H.K. Kong, H.Q. Yu, T.C. Lau, M.H. W. Lam, Photoassisted fenton degradation of polystyrene, Environ. Sci. Technol. 45 (2011) 744–750, https://doi.org/10.1021/ES102182G/SUPPL_FILE/ES102182G_SI_001.PDF.
[85] Q. Gao, G. Wang, Y. Chen, B. Han, K. Xia, C. Zhou, Utilizing cobalt-doped materials as heterogeneous catalysts to activate peroxymonosulfate for organic pollutant degradation: a critical review, Environ. Sci. Water Res. Technol. 7 (2021) 1197–1211, https://doi.org/10.1039/D0EW01042A.
[86] Z. Liu, R. Ma, M. Osada, K. Takada, T. Sasaki, Selective and controlled synthesis of α- and β-cobalt hydroxides in highly developed hexagonal platelets, J. Am. Chem. Soc. 127 (2005) 13869–13874, https://doi.org/10.1021/JA0523338/SUPPL_FILE/JA0523338SI20050729_061103.PDF.
[87] J.R.S. Brownson, C. Lévy-Clément, Nanostructured α- and β-cobalt hydroxide thin films, Electrochim. Acta. 54 (2009) 6637–6644, https://doi.org/10.1016/j.electacta.2009.06.034.
[88] V.A.M. Brabers, A.D.D. Broemme, Low-spin-high-spin transition in the Co3O4 spinel, J. Magn. Magn. Mater. 104–107 (1992) 405–406, https://doi.org/10.1016/0304-8853(92)90853-G.
[89] R. Bhargava, S. Khan, N. Ahmad, M.M.N. Ansari, Investigation of structural, optical and electrical properties of Co3O4 nanoparticles, AIP Conf. Proc. 1953 (2018), 030034, https://doi.org/10.1063/1.5032369.
[90] H. Li, Y. Zhou, W. Tu, J. Ye, Z. Zou, State-of-the-Art progress in diverse heterostructured photocatalysts toward promoting photocatalytic performance, Adv. Funct. Mater. 25 (2015) 998–1013, https://doi.org/10.1002/ADFM.201401636.
[91] K.E. O'Shea, D.D. Dionysiou, Advanced oxidation processes for water treatment, J. Phys. Chem. Lett. 3 (2012) 2112–2113, https://doi.org/10.1021/JZ300929X.
[92] H. Wang, Y. Wu, T. Xiao, X. Yuan, G. Zeng, W. Tu, S. Wu, H.Y. Lee, Y.Z. Tan, J. W. Chew, Formation of quasi-core-shell In2S3/anatase TiO2@metallic Ti3C2Tx hybrids with favorable charge transfer channels for excellent visible-light-photocatalytic performance, Appl. Catal. B Environ. 233 (2018) 213–225, https://doi.org/10.1016/j.apcatb.2018.04.012.
[93] G. Cohen, R.E. Heikkila, The generation of hydrogen peroxide, superoxide radical, and hydroxyl radical by 6 hydroxydopamine, dialuric acid, and related cytotoxic agents, J. Biol. Chem. 249 (8) (1974) 2447–2452.
[94] T. An, J. An, H. Yang, G. Li, H. Feng, X. Nie, Photocatalytic degradation kinetics and mechanism of antivirus drug-lamivudine in TiO2 dispersion, J. Hazard. Mater. 197 (2011) 229–236, https://doi.org/10.1016/j.jhazmat.2011.09.077.